



HAL
open science

In-Line X-Ray Phase Tomography of Bone and Biomaterials for Regenerative Medicine

Max Langer

► **To cite this version:**

Max Langer. In-Line X-Ray Phase Tomography of Bone and Biomaterials for Regenerative Medicine. Alessandra Giuliani; Alessia Cedola. *Advanced High-Resolution Tomography in Regenerative Medicine. Three-Dimensional Exploration into the Interactions between Tissues, Cells, and Biomaterials*, 26 (9), Springer International Publishing, pp.91-109, 2018, *Fundamental Biomedical Technologies*, 978-3-030-00367-8. 10.1007/978-3-030-00368-5_6 . hal-02058798

HAL Id: hal-02058798

<https://hal.science/hal-02058798>

Submitted on 2 Oct 2023

HAL is a multi-disciplinary open access archive for the deposit and dissemination of scientific research documents, whether they are published or not. The documents may come from teaching and research institutions in France or abroad, or from public or private research centers.

L'archive ouverte pluridisciplinaire **HAL**, est destinée au dépôt et à la diffusion de documents scientifiques de niveau recherche, publiés ou non, émanant des établissements d'enseignement et de recherche français ou étrangers, des laboratoires publics ou privés.

In-Line X-Ray Phase Tomography of Bone and Biomaterials for Regenerative Medicine

Max Langer

The aim of this chapter is to present recent developments in X-ray tomography using in-line phase contrast and their applications to mineralised tissue, whether bone or artificial biomaterials, at micro- and nanoscale. Recently, the main efforts in reconstruction algorithms for in-line X-ray phase contrast imaging have been to push resolution towards the nanoscale and extend the possibilities for quantitative imaging to more general objects. The first is made possible by the use of X-ray optics and the second by the introduction of more advanced priors in the reconstruction. We summarise here these developments and outline recent applications of these techniques, namely, nano-tomography of the ultrastructure of bone and micro-tomography of bone formation in artificial bone grafts as well as in healthy growing mice. While still relatively little used in the field of regenerative medicine, we hope that these examples will stimulate further studies in this field.

1 Introduction

X-ray computed tomography on the micrometric scale (μ CT) is nowadays a standard technique in the characterisation of biological materials such as bone [1–5]. Due to the penetrative nature of X-rays, it is ideally suited to study hard, opaque tissues. It is a 3D technique, which allows the precise study of certain structures such as trabecular bone, vessels, collagen texture and osteocyte lacunae without the need to resort to stereology. Further, if a sufficiently monochromatic beam is used, it is a quantitative technique permitting densitometric imaging [6]. This is of special

M. Langer (✉)
Creatis, CNRS UMR 5220, INSERM U1206, INSA-Lyon,
Université Claude Bernard Lyon 1, Université de Lyon, Villeurbanne, France
e-mail: max.langer@creatis.insa-lyon.fr

interest in the study of regenerative medicine, since characterisation of, for example, bone healing is tantamount to evaluating the progression of mineralisation in the newly formed bone tissue.

These properties make X-ray μ CT a prime candidate as a characterisation tool in biomaterial research and regenerative medicine, especially in the case of mineralised tissue. The specific challenges of imaging such samples have proven somewhat limiting, however, due to insufficient sensitivity of X-ray μ CT. Often, the structures of interest are lowly contrasted, for example, small mineralisation gradients in forming bone, or vessels, fat and other soft tissues embedded in hard tissues such as bone or mineralised scaffolds. A concrete example is the imaging of 3D cultures of bone cells on a mineralised substrate, where ideally newly formed bone, pre-bone matrix, bone cells, vessels as well as mineralisation of bone and substrate should be quantified. This application will be discussed more in detail below.

While certain structures, e.g. vessels, can be enhanced by the use of contrast agents [7, 8], this often poses the risk of altering the structure to be imaged. One way to increase the sensitivity of X-ray μ CT is to use phase contrast [9]. While several ways of achieving X-ray phase contrast exist [10–15], if a sufficiently coherent source, such as a synchrotron, is used, X-ray phase contrast can be achieved simply by placing the detector a small distance away from the sample [16]. The contrast thus achieved is due to Fresnel diffraction. The resulting imaging modality can be several orders of magnitude more sensitive than standard (attenuation-based) X-ray imaging depending on the material (particularly in soft tissue, the contrast is enhanced). To achieve a quantitative imaging modality, an additional reconstruction step has to be performed, however: to reconstruct the phase shift in the object from the Fresnel diffraction phase contrast images through a process known as phase retrieval [17]. The resulting phase images can then be used in conjunction with tomographic imaging to create 3D reconstructions of the refractive index and by extension the mass density distribution in the object.

Here, we will show the latest developments of X-ray phase contrast μ CT relevant to imaging in regenerative medicine and recent applications. Nano-tomography of bone ultrastructure shows great promise for the analysis of cellular structure as well as collagen and mineral distribution at the ultrastructural level. So far only the proof of concept has been reported, but the technique should provide plenty of opportunity for studies, e.g. of bone healing and pathology [18–24]. In micro-tomographic imaging, newly developed reconstruction algorithms have provided unprecedented insight in bone formation in healthy growing mice [25] and in bone cell culture in mineralised 3D substrates [26].

2 Method

When an X-ray beam passes through an object, it is mainly affected in two ways: it might be absorbed in the object (through the photoelectric effect), which changes its amplitude, and it might be retarded in the object, which changes its phase. For

X-rays we can consider the object completely described by the complex refractive index. Both the attenuation and the phase shift induced by the object can be described as projections through the absorption and refractive index distributions. This means that both parts of the complex refractive index can be reconstructed by tomographic reconstruction if amplitude and phase can be measured or reconstructed for different angular settings of the sample.

For the relatively short propagation distances we are interested in here, usually up to 1 m, the effect of propagation on the exit wave field can be described in the framework of Fresnel diffraction. Such an image is referred to as a Fresnel diffraction pattern or a phase contrast image. Intensity is measurable in essentially every plane downstream of the object, but the phase shift is lost and has to be reconstructed from intensity images. There is a quantitative but non-linear relationship between the induced phase and the contrast.

We can distinguish two distinct imaging setups: one for phase contrast μ CT and one for nano-CT.

In-line X-ray phase contrast μ CT uses essentially the same imaging setup as μ CT but with the detector mounted on a translation stage, or fixed at a position downstream of the sample stage, to permit the free space propagation necessary for the phase contrast fringes to become visible [27] (Fig. 6.1a). This setup is limited in resolution by the scintillating screen used to convert X-rays to visible light and the visible light microscope used to image the scintillating screen onto the CCD camera. This gives a diffraction-limited resolution of ~ 400 nm depending on the wavelength of the light emitted by the scintillator. This is the same resolution limit as in visible light microscopy-based techniques such as histology and histomorphometry.

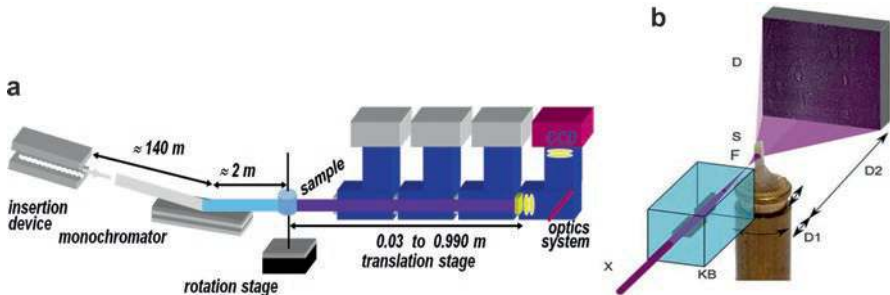


Fig. 6.1 Imaging setups in synchrotron radiation propagation-based phase contrast imaging. (a) In X-ray microscopy, X-rays are taken from an insertion device and then optionally monochromatised depending on the application. The long source to sample distance yields a high degree of spatial coherence necessary for good phase contrast fringe visibility. The sample is mounted on a translation-rotation stage (standard SR- μ CT setup). The detector, consisting of a scintillator, light microscope optics and a CCD, is mounted on a translation stage to allow for free space propagation of the beam after the sample. (b) In nanoscopic imaging, the incoming (parallel) X-ray beam is first focused into a focal spot using reflective optics. The sample is placed between the focal spot and the detector in the resulting divergent beam to create geometric magnification. The sample is placed on a translation stage (with the detector position kept fixed) to vary the propagation distance and magnification [18]

X-ray in-line nano-tomography uses X-ray reflective (Kirkpatrick-Baez) optics to focus the X-ray beam [28]. The sample is then placed behind the focus in the resulting divergent beam (Fig. 6.1b). This setup achieves geometric magnification (projection microscopy) on the X-ray side. The image formed on the scintillator is thus already magnified and is then further magnified by the visible light optics. This setup is in theory diffraction limited by the wavelength of the X-rays (0.1–1 nm for hard X-rays) and in practice limited by the quality of the X-ray optics and the stability of the imaging setup.

In the microscopic case, the recorded images can be used directly as input to a tomographic reconstruction algorithm [29]. This gives rise to images that are enhanced at the interfaces between different materials in the sample. This is roughly a superposition of the standard (attenuation) tomogram and the second derivative of the real part of the 3D complex refractive index distribution and is often called edge-enhancement tomography or sometimes simply phase contrast tomography. In nano-tomography, due to the high resolution and the resulting relatively long propagation distance, the phase contrast fringes are much too delocalised to be useful in direct reconstruction [28]. Here, phase retrieval becomes a mandatory step to achieve useful images.

While edge-enhanced imaging can be an interesting technique in its own right, it is often more interesting to consider the quantitative (but non-linear) relationship between phase shift induced on the beam by the object and the resulting phase contrast. This relationship can be used to reconstruct the phase shift at the exit of the sample through a process usually called phase retrieval. Phase retrieval is a non-trivial, non-linear inverse problem and is still the subject of active research [30–38]. We focus here on two recent developments of particular interest for imaging in regenerative medicine, namely, extension of linear phase retrieval algorithms to include multi-material and heterogeneous objects [30, 39] and the use of a non-linear conjugate gradient method to improve the resolution in the reconstruction [18].

Due to the physics of the image formation, the transfer of information from phase to contrast in the low spatial frequency range is low (this can be understood, e.g. through observing that the phase contrast is approximately proportional to the second derivative of the phase shift, as mentioned above). Because of this, the reconstructed refractive index can be affected by strong low-frequency noise [40]. This can strongly inhibit the possibility to quantitatively analyse the reconstructed samples. This kind of artefact has been handled by introducing information in the low frequency range from the measured attenuation [41, 42].

By assuming that the object is homogeneous, the phase (and equivalently the attenuation, considering strict proportionality between attenuation and phase) can be estimated from a single phase contrast image [41]. This has proven to be a very successful method due to the facility of using a single phase contrast image. Great care must be taken when imaging heterogeneous objects, however, especially if quantitative (densitometric) results are required: the ratio between the real (related to phase) and imaginary (related to attenuation) part of the refractive index must vary within a narrow range, and a careful calibration must be performed to correct for the bias introduced by the homogeneity assumption [43].

A more recent development seeks to overcome the limitation of homogeneous objects by using an attenuation tomogram as prior knowledge on the low spatial

frequencies of the phase [30, 39]. A tomographic scan at a short distance (depending on the resolution; short enough that phase contrast fringes are not too visible) is reconstructed and then processed in various ways to achieve an estimate of the low spatial frequencies of the real part of the refractive index. This new volume is then forward projected and used as a prior in a least square minimisation problem to retrieve the phase. This approach has some advantages, namely, it is quantitative even for non-homogeneous objects (not for all objects, however; it is somewhat dependent on the composition. Some materials, for example, bone, show a convenient quantitative, non-linear functional relationship between attenuation and phase). It also permits (somewhat paradoxically) to reduce the imaging dose by recording images at several distances, fractioning the dose between the images [44]. The disadvantages, on the other hand, are the increased complexity of using several distances. Each sample requires somewhat longer total acquisition time (due to camera displacements; the exposure time can actually be reduced for a given final image quality) and more storage space, and the images at each projection angle have to be realigned through image registration (albeit this problem has been thoroughly addressed in literature) [45]. Also, this method can clearly not be used in in situ and high frame rate imaging due to the requirement of images at several distances.

The two approaches mentioned above are based on linearised versions of the forward problem, however. In high-resolution imaging (approximately $<1 \mu\text{m}$ in practice), the non-linear contributions start to be important. This presents itself mainly as a loss of resolution. Several methods to overcome this problem have been suggested [18, 33, 34, 46, 47]. The most successful so far seems to be the method based on a non-linear conjugate gradient algorithm [18]. This algorithm must be initialised with a reconstruction sufficiently close to the desired reconstruction, usually with a reconstruction using a linear algorithm, to yield good results. It has been shown to improve resolution of the reconstructions in the nano-tomography case, although there is no reason to believe it should not improve image quality in the microscopic case as well. This would be achieved at the cost of a substantially increased computation time (albeit fully acceptable using current computational resources: currently around 10 min per projection, fully parallelisable over the projections due to the independence of the projections in tomographic imaging). It should be noted that this type of algorithm does not seem to improve the low spatial frequency content of the images. Regularisation-based methods such as the ones mentioned above seem to be mandatory to resolve this problem.

3 Applications

3.1 *Nano-tomography of Bone*

Nano-tomography has proven to be a very interesting imaging modality for bone imaging. This is due to the ability of X-rays to image the otherwise opaque material in 3D coupled with the ability to reach resolutions below 100 nm, which is important for the imaging of the osteocyte network, which presents structures down to

approximately 100 nm [48]. While imaging of the osteocyte network was the first intended application, the first in-line nano-tomography study of bone revealed that the high sensitivity of the technique made possible to also study the collagen structure of bone, as well as mineralisation on the <100 nm length scale [20, 48].

3.1.1 Analysis of Collagen Structure

Effectively, the lacuno-canalicular network (LCN) can be imaged over a relatively large field of view (Fig. 6.2) with very good spatial resolution. The bone matrix appears strongly textured, showing an arching structure (Fig. 6.2a–c). This arching structure can be identified, by comparison to qBEI [49] and TEM [50] images, to be due to the oblique virtual cutting of the mineralised collagen fibrils. The texture due to the collagen fibrils is sufficiently contrasted to be studied directly in 3D using texture analysis [19].

Using this technique, it can be seen that the mineralised collagen fibrils in this sample are organised in a plywood structure, consisting of parallel quasi-planes, where the fibrils have the same alignment. The collagen structure in bone has been hypothesised to act as a crack arresting boundary and thus protect vessels and nerves embedded in canals within the bone [51]. A qualitative validation of the texture analysis can be performed by constructing a virtual 3D fibril model, where the local orientation is represented by cylindrical stream lines. This model compares well with the corresponding sub-volume of the original greyscale image. The arch pattern is clearly reproduced (Fig. 6.3). This illustrates the necessity of 3D analysis: the complex arrangement of the collagen fibrils cannot be retrieved from 2D sections.

3.1.2 Finite Element Modelling of Osteocytes

The porosity in bone is at least as important as the tissue matrix itself, both biologically and mechanically. In cortical bone, on the micrometric scale, the pore network is formed by the osteocyte lacunae hosting the cell bodies and the canaliculi (small tunnels connecting lacunae of neighbouring cells [52, 53]. Given the presumed importance of the osteocyte in the coordination of other bone cells and in remodeling [54, 55], the LCN has recently received increasing attention. Imaging of this pore network is an important, but not yet fully solved challenge.

An unresolved issue with the LCN was the difference in strain affecting bone in vivo (thousands microstrains) [56] and the strain required to stimulate osteocytes in vitro (tens of thousands of microstrains) [57]. One hypothesis is that there is a “strain amplification mechanism” affecting the osteocytes for them to sense deformation, for example, through the morphology of the LCN.

To test this hypothesis, in-line phase tomography was used to image human femoral cortical bone. Imaging provided volumes with 102 μm field of view and 50 nm voxel size. Rectangular volumes of interest (VOIs) were selected from the images to analyse the LCN and deformations of osteocytes. Each VOI contained a single

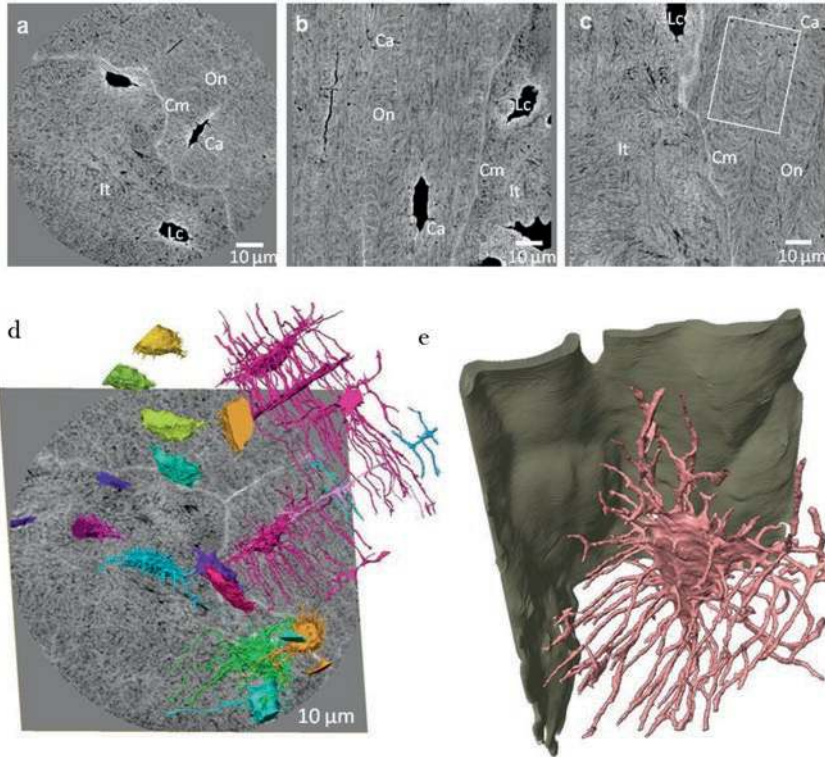


Fig. 6.2 Nano-tomography of bone. (a–c) Virtual cuts through human cortical bone. The LCN is exceptionally well contrasted. The strongly contrasted arching structure in the matrix presumably due to oblique cutting of the mineralised collagen fibres, as well as well-resolved cement lines. (d) Volume rendering of all LCN porosity in a tomogram showing a relatively large number of lacunae. (e) Zoom on one lacuna and its canaliculi (pink) and the cement line (green). The LCN is rendered in unprecedented detail. The spatial relationship to structures such as the cement line can be studied

lacuna with its canaliculi (Fig. 6.4a). The geometry of the pores was extracted using an ad hoc segmentation algorithm using thresholding, morphological operations and a connectivity enhancement algorithm [58]. In each VOI, the lacuna and canaliculi were separated into two distinct compartments, and several morphological parameters of both were quantified (Fig. 6.4b). These included volumes, surfaces, descriptors of shape as well as number, diameter and spacing of canaliculi.

Case-specific finite element models of the VOIs were created. The models included the extracellular matrix surrounding the pores, the pericellular soft tissue matrix in the lacuna and the canaliculi, as well as the cell body and processes of the osteocyte (Fig. 6.4c). The osteocytes are not directly visible in the images. Therefore, the extent of the cells was extrapolated based on observations using electron microscopy [59, 60]. Material properties were modelled as linear elastic and isotropic, with parameters assigned based on literature data [61]. A confined

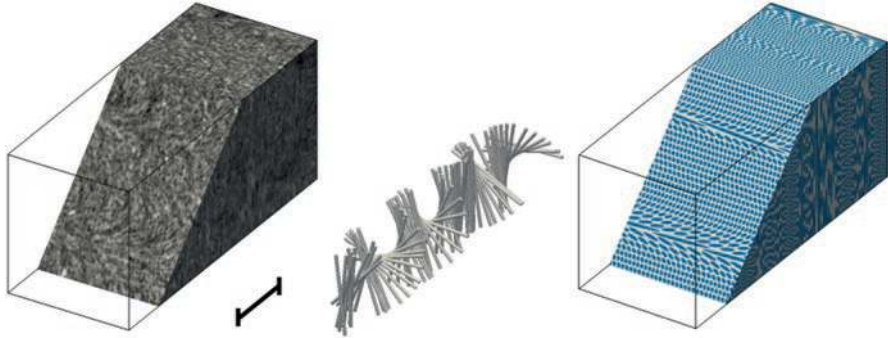


Fig. 6.3 Qualitative validation of a texture analysis approach to quantify mineralised collagen fibril orientation. Left: crop of a nano-CT image of a human femoral cortical bone. Grey values represent the inverted mass density in arbitrary units. Scale bar: 10 μm . Middle: cylinders representing the measured fibril orientation if 600 μm thick sections along one line. Right: 3D image generated based on extracted orientations with the fibrils shown in blue and the matrix in white. The arc pattern in the oblique cut corresponds well to that in the original image (left)

uniaxial compressive deformation along the direction the longest lacunar dimension was simulated in the models, with magnitude set to the physiologically relevant 1000 microstrains [56].

The finite element analysis showed that the magnitude of the strain at the dendrite/cell body junction reached up to 70 times the externally applied deformations, and further local peaks were observed in the dendrites (Fig. 6.4d). Resulting strain magnitudes are in the range reported to stimulate osteocytes in vitro [57]. This means that the shape of the osteocytes contribute to a strain amplification effect. The case-specific models predicted higher strain amplification factors compared not only to idealised ones [62–64] but also to previously reported case-specific simulations using either a different image source [61] or a less fine modelling approach [65].

3.2 In-Line Phase Micro-tomographic Imaging of Bone Formation

A very interesting application of in-line X-ray phase contrast tomography is the imaging of mineralised three-dimensional porous biomaterials used as scaffolds in bone tissue engineering and more generally for 3D bone cell culture [66, 67]. The desired properties of these biomaterials are a surface favourable for cell attachment, that they stimulate bone cell precursors to differentiate into mature bone cells and that they can contribute to bone regeneration [68]. They should also be resorbable by the receiving body and be replaced by new, living bone. While bone formation and resorption can, to a certain extent, be quantified by SR- μCT and microdiffraction [69, 70], these techniques lack the sensitivity to resolve soft and weakly mineralised tissue. Imaging of soft tissue in mineralised scaffolds is challenging due to the

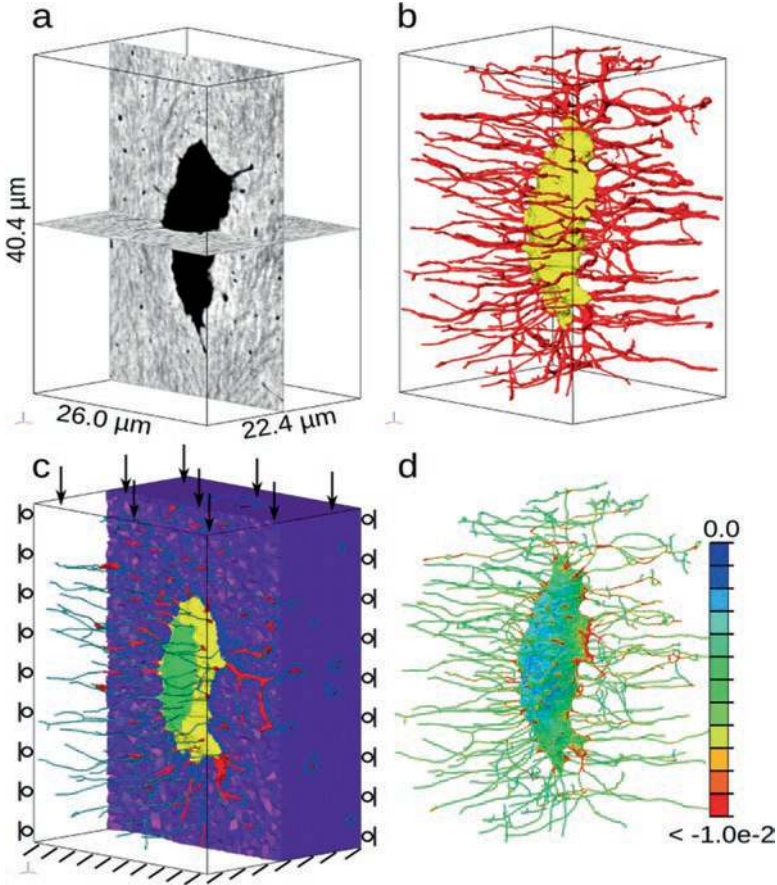


Fig. 6.4 Quantification of lacunar-canalicular morphology and simulation of strains on the osteocyte. **(a)** One lacuna and associated canaliculi cropped from the nano-CT image. **(b)** Surface rendering of the segmented lacuna (yellow) and canaliculi (red). **(c)** Finite element mesh of the mineralised extracellular matrix (purple and blue), the pericellular soft tissue (yellow) and the canaliculi (red), the cell body (light green) and processes (turquoise). The latter two were inferred based on literature data. Parts of the model are transparent to allow visualisation of all compartments. The direction of the compression of 1000 microstrains is also shown. **(d)** Minimum (compressive) principal strain on the osteocyte by FEM, showing peaks in the deformation (red: >10,000 microstrains, a strain amplification of at least 10 times) at the junctions of the dendrites and cell body as well as at certain locations of the dendrites further away from the lacuna

opacity of the structure to visible light and the necessary trade-off between sufficient penetration and attenuation of X-rays to achieve the necessary sensitivity using standard μ CT. Quantification of soft tissue formation is important for the characterisation of such biomaterials, since it constitutes the sites where new bone formation is possible. The increased sensitivity of phase tomography, however, has enabled the analysis of soft tissues in mineralised scaffolds [71]. Further, different soft tissues can be differentiated in the images, such as collagen, fat, vessels and cells [26].

3.2.1 Imaging of Mineralised Bone Scaffolds Cultured with Bone Cells In Vitro

As an illustration, we show the imaging of Skelite bone scaffolds seeded with human osteoblasts. Skelite is a porous biomaterial consisting of 67% silicon-stabilised tricalcium phosphate (Si-TCP) and 33% hydroxylapatite (HA). It has an open pore structure similar to human cancellous bone, with a pore size between 200 and 500 μm and a porosity level around 60% [72, 73]. Disks of Skelite measuring 9 mm in diameter and 1.2 mm in thickness were seeded with osteoblasts and cultured for 8 weeks. Samples were washed in phosphate-buffered saline, fixed in paraformaldehyde, stored in 70% ethanol and then dried before imaging. The samples were mounted three and three in a Perspex cylinder, separated by fibre tissue paper and lightly compressed with a foam material to take advantage of the 7 mm vertical field of view.

Imaging was performed using undulator radiation monochromatised to 30 keV using a single Si crystal monochromator. A 10 μm Gadox scintillating screen, standard light microscope optics and a FreLoN CCD camera were used for detection, set to yield a pixel size of 5 μm . Tomographic data sets comprising 2000 angles of view over a 180° rotation were recorded over 3 distances (0.01, 0.33 and 0.99 m), with an exposure time of 0.4 s. Phase retrieval was performed using a multi-material prior. The two δ/β -ratios were calculated using the XOP software and set to 335 for Skelite and 2000 for soft tissue.

The reconstruction is shown in (Fig. 6.5). Attenuation and phase tomograms are shown to illustrate the increased visibility of the soft tissue in the phase tomogram. This enables segmentation, visualisation (Fig. 6.5d) and quantitative analysis (such as volume, volume filling fraction and local thickness) of the soft tissue phase. Additionally, sensitivity was sufficiently high to permit segmentation of the osteoblasts. These types of measurements can be used to evaluate the osteoconductive and osteoinductive properties of different scaffold types, as well as the impact of different culture conditions, for example, different biochemical environments or microgravity.

3.2.2 Imaging of Forming Bone in Young Mice

The sensitivity of X-ray phase contrast imaging permits to reveal the main characteristics of the important tissue compartments in forming bones, including the rapidly changing soft tissue and the partially or fully mineralised bone regions, while revealing subtle density differences in 3D. Growing femur bone midshafts of healthy mice at 1, 3, 7, 10 and 14 days postpartum were imaged. It was possible to create exquisitely detailed maps of the juxtaposed soft, partially mineralised and highly mineralised bone, giving insight into the environment in which bone cells create and shape the bone matrix [25].

Growing bone exhibits a complex architecture in 3D, which undergoes extensive reorganisation and restructuring, from the initially deposited bone material to the mature bone. Consequently, these forming tissues exhibit a range of very dif-

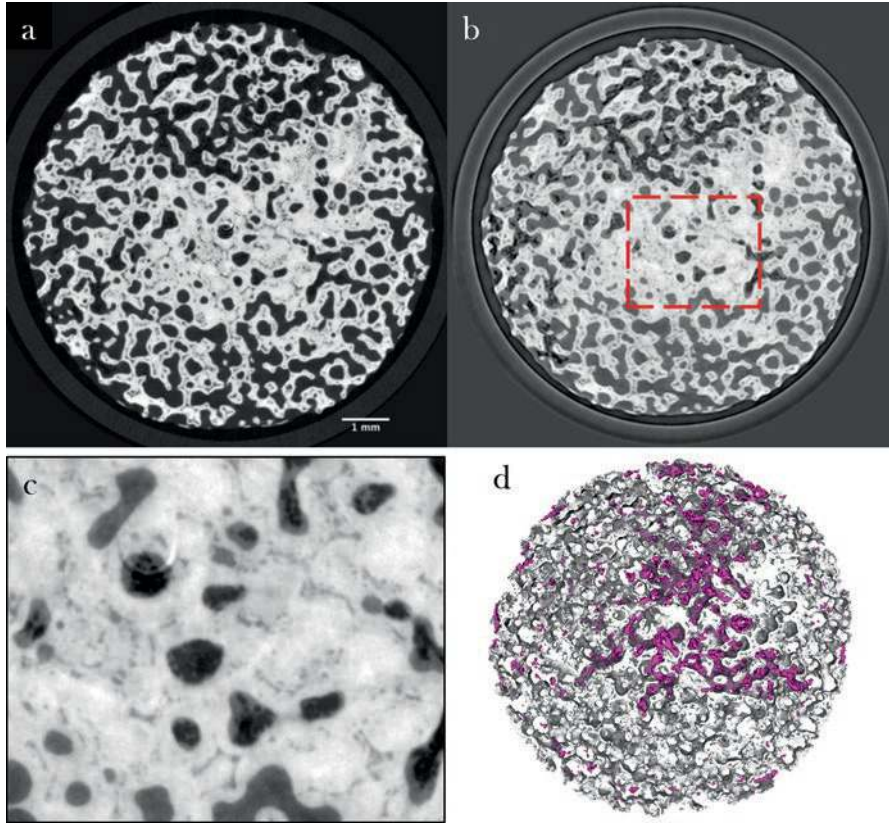


Fig. 6.5 Phase μ CT imaging of mineralised scaffolds. (a) Standard μ CT image of a Skelite disk seeded with osteoblasts. (b) Phase tomogram of the same disk, showing clearly the deposited soft tissue. It can be seen that soft tissue is formed mainly inside the scaffold construct and that the volume filling fraction is high. (c) Zoom on the marked area in (b). There is sufficient contrast to segment not only scaffold and soft tissue but the osteocytes as well. (d) Rendering of the scaffold and the segmented osteocytes

ferent morphologies. Different morphologies can be observed in the same skeleton during growth or healing, for example, following fracture or biomaterial implantation. When non-mineralised osteoid matrix starts to mineralise, bone material in both formation and healing conditions appears as a highly porous structure, where mineralised and soft tissues are intermixed. Such early formed bone tissues gradually transform and rearrange into solid cortical bone that eventually takes on the appearance of the mature tissue [74–81]. The initial tissue morphology is transient and contains zones of markedly different morphologies. Different degrees of mineralisation can be observed in adjacent sites at the same time. Due to the dynamically changing tissue geometry, mechanical properties are difficult to define and measure. Detailed information about both architecture and density is thus necessary for understanding and possibly predicting bone growth and tissue repair.

In-line phase tomography was used for the quantification and characterisation of the temporal evolution of morphology and mineralisation during bone genesis in healthy mice. The left femur was dissected from female wild-type C57BL/6 mice aged 1, 3, 7, 10 and 14 days after birth. Skin and muscle was partially removed, while the bones remained intact. Samples were fixed and stored in 70 wt% ethanol at 4 °C. The samples were imaged in an ethanol atmosphere, mounted within small polypropylene cylindrical vials. A filtered “pink” X-ray beam at 26 keV was used to record tomographic scans of 3999 images at five sample-to-detector distances with an exposure time of 100 ms per image. The detector was a custom-made indirect system consisting of a 10×/0.3NA Olympus objective combined with a thin-single crystal scintillator and a pco.edge sCMOS camera [82]. Phase retrieval was performed using the multi-material algorithm outlined in Sect. 2, with a delta-to-beta ratio of 429.9 in mineralised bone and 1857 elsewhere. The local mass density can be accessed through a simple scaling of the resulting phase tomograms [18].

Histogram analysis was used to calibrate slight offsets in the background (air) in the density data [20]. The images were segmented into bone and soft tissue compartments using standard thresholding [81]. 3D renderings were performed using CTvox (Bruker-microCT, Kontich, Belgium) by mapping colour and transparency in the transfer functions to tissue density.

Renderings are shown in Fig. 6.6, where blue represents soft tissue, green represents bone and red represents very high density within the bone (presumably mineralised cartilage). Cutouts are shown to reveal what would be masked by the encasing soft tissue. During development, the 3D distribution of mineralised material changes from a loosely connected foam-like structure (1–7 days) into a condensed bone cortex, sandwiched between soft tissue layers. High-density islands (possibly mineralised cartilage) seem to be encapsulated within the bone compartment.

The mineralised tissue only is shown in Fig. 6.7. The cortical bone develops from a highly porous scaffold consisting of mineralised struts into the mature solid ring seen in the samples obtained from 14-day-old animals. It can be seen in the high-resolution cutouts that the bone morphology changes extensively during maturation, through a redistribution of high-density regions located within the lower-density bone.

In addition to the qualitative morphological information, the phase tomograms permit quantification of 3D local mass density. The soft tissue was measured to have a density of 1.1–1.4 g/cm³ at all ages. These values are slightly higher than published values for soft (skeletal) tissue (1.0–1.06 g/cm³) [25]. The observed higher values could be due to higher concentrations of mineral precursor phases in the soft tissue. Higher density has similarly been revealed by other methods in forming bone tissue [18, 71, 76, 83]. The amount of bone increases with increasing age and contains a high-density component, presumably mineralised cartilage [84–86], much of which is later replaced with less dense material (bone).

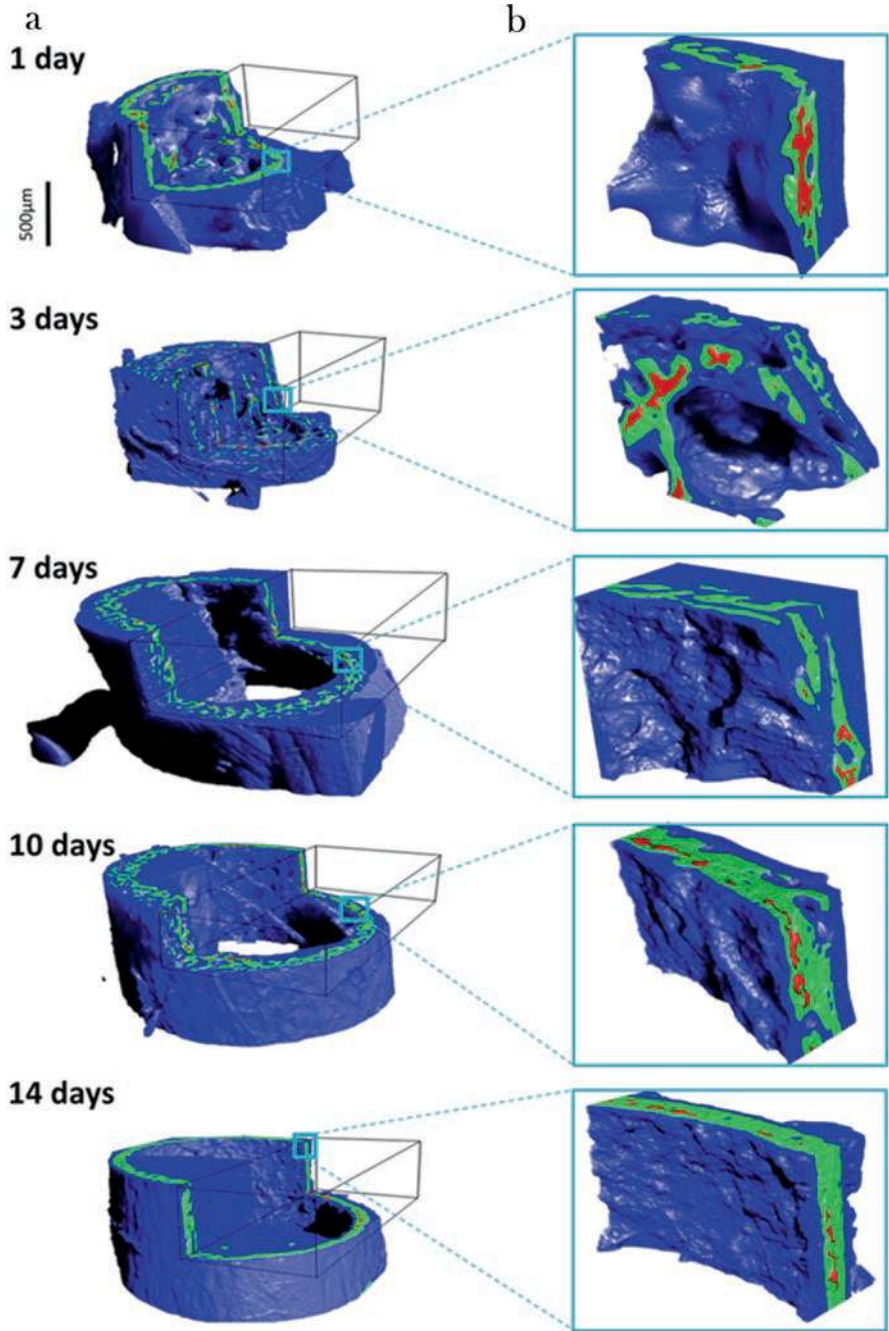


Fig. 6.6 Renderings of the mass density distribution in growing mouse femurs at different time points. (a) Soft tissue (blue) surrounds the mineralised bone (green). Islands of high mineral density (presumably mineralised cartilage) exceeding 1.9 g/cm^3 (red) can be seen. (b) The denser islands can be better observed on magnified cutouts

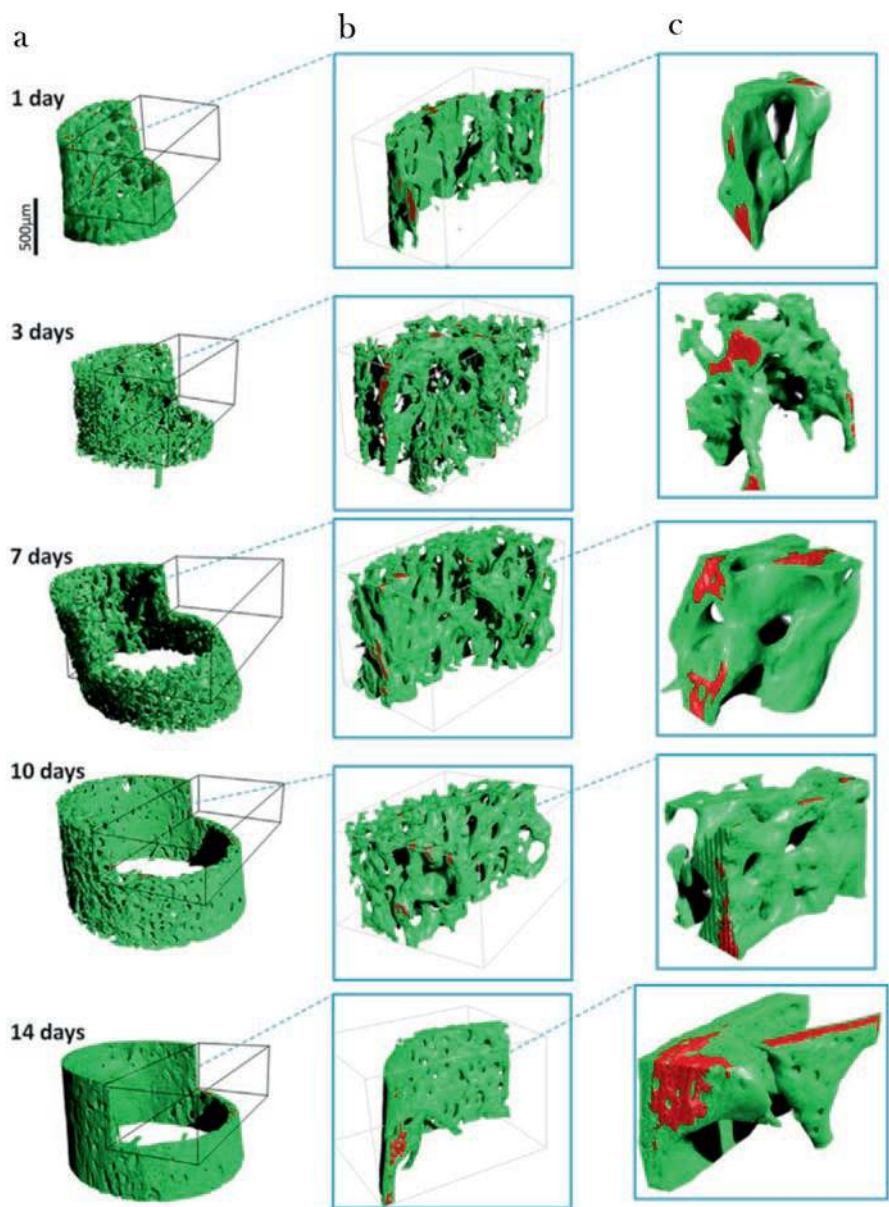


Fig. 6.7 3D renderings of the mineralised tissue only from Fig. 6.6. Bone (green) and high-density zones (red) with increasing magnifications (a–c) are shown. The high mass density (exceeding 1.9 g/cm^3) is always found within regions of lower density. Note the drastic architectural changes from 1 to 14 days, changing from a foam-like open network to a solid tube-like cortical structure

4 Perspectives

There is a growing interest in phase sensitive X-ray imaging methods in regenerative medicine. This is mainly motivated by the high resolution and sensitivity offered by the technique. We presented here examples of imaging studies using phase tomography: nano-tomography of bone and micro-tomography of growing bone in healthy growing mice and in artificial bone constructs. Similar approaches could be used to study bone tissue growth and maturation in adult animals, during healing. Indeed, much remains unknown about the similarities and differences in the 3D bone tissue dynamics when comparing bone growth/genesis and fracture and tissue healing, for example, in response to implantation of biomaterials. The ability to resolve fine density variations in different tissues might allow the elucidation of the bone formation process in the tissue engineering scenario.

References

1. Bonse U (2002) Developments in X-ray tomography II. Proc. of SPIE 4503
2. Bouxsein ML, Boyd SK, Christiansen BA, Guldberg RE, Jepsen KJ, Müller R (2010) Guidelines for assessment of bone microstructure in rodents using micro-computed tomography. *J Bone Miner Res* 25(7):1468–1486
3. Engelke K, Karolczak M, Lutz A, Seibert U, Schaller S, Kalender W (1999) Micro-CT. Technology and application for assessing bone structure. *Radiologe* 39(3):203–212
4. Hildebrand T, Laib A, Müller R, Dequeker J, Rüegeegger P (1999) Direct three-dimensional morphometric analysis of human cancellous bone: microstructural data from spine, femur, iliac crest, and calcaneus. *J Bone Miner Res* 14(7):1167–1174
5. Salomé M et al (1999) A synchrotron radiation microtomography system for the analysis of trabecular bone samples. *Med Phys* 26(10):2194
6. Nuzzo S, Peyrin F, Cloetens P, Baruchel J, Boivin G (2002) Quantification of the degree of mineralization of bone in three dimensions using synchrotron radiation microtomography. *Med Phys* 29:2672–2681
7. Langer M, Prisby R, Peter Z, Guignandon A, Lafage-Proust M-H, Peyrin F (2011) Simultaneous 3D imaging of bone and vessel microstructure in a rat model. *IEEE Trans Nucl Sci* 58(1):139–145 . PART 1
8. Prisby R et al (2011) Intermittent PTH 1-84 is osteoanabolic but not osteoangiogenic and relocates bone marrow blood vessels closer to bone forming sites. *J Bone Miner Res* 26(11):2583–2596
9. Momose A, Takeda T, Itai Y, Hirano K (1996) Phase-contrast X-ray computed tomography for observing biological soft tissues. *Nat Med* 2(4):473–475
10. Zanette I et al (2013) Holotomography versus X-ray grating interferometry: a comparative study. *Appl Phys Lett* 103:244105
11. Lang S et al (2014) Experimental comparison of grating- and propagation-based hard X-ray phase tomography of soft tissue. *J Appl Phys* 116(15):154903
12. Varga P, Weber L, Hesse B, Langer M (2016) Synchrotron X-ray phase nanotomography for bone tissue characterization. In: X-ray and neutron techniques for nanomaterials characterization. Springer Berlin Heidelberg, Berlin/Heidelberg, pp 1–42

13. Langer M, Boistel R, Pagot E, Cloetens P, Peyrin F (2010) X-ray in-line phase microtomography for biomedical applications. In: Méndez-Vilas A, Díaz J (eds) *Microscopy: science, technology, applications and education*, vol 1., no. 4. Formatex Research Center, Badajoz, pp 391–402
14. Hagen CK et al (2015) High contrast microstructural visualization of natural acellular matrices by means of phase-based x-ray tomography. *Sci Rep* 5:18156
15. Bravin A, Coan P, Suortti P (2013) X-ray phase-contrast imaging: from pre-clinical applications towards clinics. *Phys Med Biol* 58(1):R1–R35
16. Snigirev A, Snigireva I, Kohn V, Kuznetsov S, Schelokov I (1995) On the possibilities of x-ray phase contrast microimaging by coherent high-energy synchrotron radiation. *Rev Sci Instrum* 66(12):5486
17. Cloetens P et al (1999) Holotomography: quantitative phase tomography with micrometer resolution using hard synchrotron radiation x rays. *Appl Phys Lett* 75(19):2912
18. Langer M, Pacureanu A, Suhonen H, Grimal Q, Cloetens P, Peyrin F (2012) X-ray phase nanotomography resolves the 3D human bone ultrastructure. *PLoS One* 7(8):e35691
19. Varga P et al (2013) Investigation of the 3D orientation of mineralized collagen fibrils in human lamellar bone using synchrotron X-ray phase nano-tomography. *Acta Biomater* 9:8118–8127
20. Hesse B et al (2014) Canalicular network morphology is the major determinant of the spatial distribution of mass density in human bone tissue – evidence by means of synchrotron radiation phase-contrast nano-CT. *J Bone Miner Res* 30(2):346–356
21. Peyrin F, Dong P, Pacureanu A, Langer M (2014) Micro- and Nano-CT for the study of bone ultrastructure. *Curr Rev Osteoporos* 12:346–356
22. Hesse B et al (2014) Accessing osteocyte lacunar geometrical properties in human jaw bone on the submicron length scale using synchrotron radiation μ CT. *J Microsc* 255(3):158–168
23. Langer M, Peyrin F (2016) 3D X-ray ultra-microscopy of bone tissue. *Osteoporos Int* 27(2):441–455
24. Giuliani A et al (2013) Three years after transplants in human mandibles, histological and in-line holotomography revealed that stem cells regenerated a compact rather than a spongy bone: biological and clinical implications. *Stem Cells Transl. Med.* 2(4):316–324
25. Bortel EL et al (2017) Combining coherent hard X-ray tomographies with phase retrieval to generate three-dimensional models of forming bone. *Front Mater* 4:39
26. Weber L, Langer M, Tavella S, Ruggiu A, Peyrin F (2016) Quantitative evaluation of regularized phase retrieval algorithms on bone scaffolds seeded with bone cells. *Phys Med Biol* 61(9):215–231
27. Cloetens P et al (1997) Observation of microstructure and damage in materials by phase sensitive radiography and tomography. *J Appl Phys* 81(9):5878
28. Mokso R, Cloetens P, Maire E, Ludwig W, Buffière J-Y (2007) Nanoscale zoom tomography with hard x rays using Kirkpatrick-Baez optics. *Appl Phys Lett* 90(14):144104
29. Cloetens P, Barrett R, Baruchel J, Guigay J-P, Schlenker M (1996) Phase objects in synchrotron radiation hard x-ray imaging. *J Phys D Appl Phys* 29(1):133–146
30. Langer M et al (2014) Priors for X-ray in-line phase tomography of heterogeneous objects. *Philos Trans A Math Phys Eng Sci* 372(2010):20130129
31. Davidoiu V, Sixou B, Langer M, Peyrin F (2013) In-line phase tomography using nonlinear phase retrieval. *Ann Univ Bucharest Math Ser* 4(LXII):115–122
32. Sixou B, Davidoiu V, Langer M, Peyrin F (2013) Absorption and phase retrieval with Tikhonov and joint sparsity regularizations. *Inverse Probl Imaging* 7(1):267–282
33. Davidoiu V, Sixou B, Langer M, Peyrin F (2014) Non-linear phase tomography based on Fréchet derivative. *Adv Comput Tomogr* 3(4):39–50
34. Ruhlandt A, Krenkel M, Bartels M, Salditt T (2014) Three-dimensional phase retrieval in propagation-based phase-contrast imaging. *Phys Rev A* 89(3):33847
35. Kostenko A, Batenburg KJ, Suhonen H, Offerman SE, van Vliet LJ (2013) Phase retrieval in in-line x-ray phase contrast imaging based on total variation minimization. *Opt Express* 21(1):710–723

36. Langer M, Cloetens P, Peyrin F (2009) Fourier-wavelet regularization of phase retrieval in x-ray in-line phase tomography. *J Opt Soc Am A Opt Image Sci Vis* 26(8):1876–1881
37. Hehn L et al (2018) Nonlinear statistical iterative reconstruction for propagation-based phase-contrast tomography. *APL Bioeng* 2(1):16105
38. Rositi H et al (2014) Computer vision tools to optimize reconstruction parameters in x-ray in-line phase tomography. *Phys Med Biol* 59(24):7767–7775
39. Langer M, Cloetens P, Pacureanu A, Peyrin F (2012) X-ray in-line phase tomography of multimaterial objects. *Opt Lett* 37(11):2151
40. Langer M, Cloetens P, Guigay J-P, Peyrin F (2008) Quantitative comparison of direct phase retrieval algorithms in in-line phase tomography. *Med Phys* 35(10):4556–4566
41. Paganin D, Mayo SC, Gureyev TE, Miller PR, Wilkins SW (2002) Simultaneous phase and amplitude extraction from a single defocused image of a homogeneous object. *J Microsc* 206(1):33–40
42. Langer M, Cloetens P, Peyrin F (2010) Regularization of phase retrieval with phase-attenuation duality prior for 3-D holotomography. *IEEE Trans Image Process* 19(9):2428–2436
43. Marinescu M et al (2013) Synchrotron radiation X-ray phase micro-computed tomography as a new method to detect Iron oxide nanoparticles in the brain. *Mol Imaging Biol* 15(5):552–559
44. Frachon T et al (2015) Dose fractionation in synchrotron radiation x-ray phase micro-tomography. *Phys Med Biol* 60(19):7543–7566
45. Weber L et al (2018) Registration of phase-contrast images in propagation-based X-ray phase tomography. *J Microsc* 269(1):36–47
46. Moosmann J, Hofmann R, Bronnikov A, Baumbach T (2010) Nonlinear phase retrieval from single-distance radiograph. *Opt Express* 18:25771–25785
47. Davidoiu V, Sixou B, Langer M, Peyrin F (2013) Nonlinear approaches for the single-distance phase retrieval problem involving regularizations with sparsity constraints. *Appl Opt* 52(17):3977–3986
48. Pacureanu A, Langer M, Boller E, Tafforeau P, Peyrin F (2012) Nanoscale imaging of the bone cell network with synchrotron X-ray tomography: optimization of acquisition setup. *Med Phys* 39(4):2229
49. Kingsmill VJ, Boyde A (1998) Mineralisation density of human mandibular bone: quantitative backscattered electron image analysis. *J Anat* 192(Pt 2):245–256
50. Giraud-Guille M-M, Besseau L, Martin R (2003) Liquid crystalline assemblies of collagen in bone and in vitro systems. *J Biomech* 36(10):1571–1579
51. Fratzl P, Weinkamer R (2007) Nature’s hierarchical materials. *Prog Mater Sci* 52(8):1263–1334
52. Schneider P, Meier M, Wepf R, Müller R (2010) Towards quantitative 3D imaging of the osteocyte lacuno-canalicular network. *Bone* 47(5):848–858
53. Currey JD, Shahar R (2013) Cavities in the compact bone in tetrapods and fish and their effect on mechanical properties. *J Struct Biol* 183(2):107–122
54. Bonewald LF (2011) The amazing osteocyte. *J Bone Miner Res* 26(2):229–238
55. Qing H et al (2012) Demonstration of osteocytic perilacunar/canalicular remodeling in mice during lactation. *J Bone Miner Res* 27(5):1018–1029
56. Group M, Hero S, Burr DB (1996) In vivo measurement of human tibial strains during vigorous activity. *Bone* 18(5):405–410
57. You L, Cowin SC, Schaffler MB, Weinbaum S (2001) A model for strain amplification in the actin cytoskeleton of osteocytes due to fluid drag on pericellular matrix. *J Biomech* 34(11):1375–1386
58. Varga P et al (2015) Strains experienced by osteocytes in situ as predicted by case specific finite element analysis. *Biomech Model Mechanobiol* 14(2):267–282
59. Anderson EJ, Knothe Tate ML (2008) Idealization of pericellular fluid space geometry and dimension results in a profound underprediction of nano-microscale stresses imparted by fluid drag on osteocytes. *J Biomech* 41(8):1736–1746
60. McNamara LM, Majeska RJ, Weinbaum S, Friedrich V, Schaffler MB (2009) Attachment of osteocyte cell processes to the bone matrix. *Anat Rec (Hoboken)* 292(3):355–363

61. Verbruggen SW, Vaughan TJ, McNamara LM (2012) Strain amplification in bone mechanobiology: a computational investigation of the in vivo mechanics of osteocytes. *J R Soc Interface* 9(75):2735–2744
62. McCreadie BR, Hollister SJ, Schaffler MB, Goldstein SA (2004) Osteocyte lacuna size and shape in women with and without osteoporotic fracture. *J Biomech* 37(4):563–572
63. Bonivitch AR, Bonewald LF, Nicoletta DP (2007) Tissue strain amplification at the osteocyte lacuna: a microstructural finite element analysis. *J Biomech* 40(10):2199–2206
64. Deligianni DD, Apostolopoulos CA (2008) Multilevel finite element modeling for the prediction of local cellular deformation in bone. *Biomech Model Mechanobiol* 7(2):151–159
65. Schneider P, Ruffoni D, Larsson D, Chiapparini I, Müller R (2012) Image-based finite element models for the investigation of osteocyte mechanotransduction. *J Biomech* 45(1):S436
66. Dorozhkin SV (2010) Calcium orthophosphates as bioceramics: state of the art. *J Funct Biomater* 1(1):22–107
67. Eliaz N, Metoki N (2017) Calcium phosphate bioceramics: a review of their history, structure, properties, coating technologies and biomedical applications. *Materials (Basel)* 10(4):334
68. Glazer PA, Spencer UM, Alkalay RN, Schwardt J (2001) In vivo evaluation of calcium sulfate as a bone graft substitute for lumbar spinal fusion. *Spine J* 11(6):395–401
69. Komlev VS et al (2006) Kinetics of in vivo bone deposition by bone marrow stromal cells into porous calcium phosphate scaffolds: an X-ray computed microtomography study. *Tissue Eng* 12(12):3449–3458
70. Cancedda R et al (2007) Bulk and interface investigations of scaffolds and tissue-engineered bones by X-ray microtomography and X-ray microdiffraction. *Biomaterials* 28(15):2505–2524
71. Langer M, Liu Y, Tortelli F, Cloetens P, Cancedda R, Peyrin F (2010) Regularized phase tomography enables study of mineralized and unmineralized tissue in porous bone scaffold. *J Microsc* 238(3):230–239
72. Sayer M et al (2003) Structure and composition of silicon-stabilized tricalcium phosphate. *Biomaterials* 24(3):369–382
73. Reid JW, Pietak A, Sayer M, Dunfield D, Smith TJN (2005) Phase formation and evolution in the silicon substituted tricalcium phosphate/apatite system. *Biomaterials* 26(16):2887–2897
74. Miller LM, Little W, Schirmer A, Sheik F, Busa B, Judex S (2007) Accretion of bone quantity and quality in the developing mouse skeleton. *J Bone Miner Res* 22(7):1037–1045
75. Manjubala I et al (2009) Spatial and temporal variations of mechanical properties and mineral content of the external callus during bone healing. *Bone* 45(2):185–192
76. Lange C et al (2011) Fetal and postnatal mouse bone tissue contains more calcium than is present in hydroxyapatite. *J Struct Biol* 176(2):159–167
77. Preininger B, Checa S, Molnar FL, Fratzl P, Duda GN, Raum K (2011) Spatial-temporal mapping of bone structural and elastic properties in a sheep model following osteotomy. *Ultrasound Med Biol* 37(3):474–483
78. Sharir A, Stern T, Rot C, Shahar R, Zelzer E (2011) Muscle force regulates bone shaping for optimal load-bearing capacity during embryogenesis. *Development* 138(15):3247–3259
79. Vetter A et al (2011) The mechanical heterogeneity of the hard callus influences local tissue strains during bone healing: a finite element study based on sheep experiments. *J Biomech* 44(3):517–523
80. Rohrbach D, Preininger B, Hesse B, Gerigk H, Perka C, Raum K (2013) The early phases of bone healing can be differentiated in a rat osteotomy model by focused transverse-transmission ultrasound. *Ultrasound Med Biol* 39(9):1642–1653
81. Bortel EL, Duda GN, Mundlos S, Willie BM, Fratzl P, Zaslansky P (2015) Long bone maturation is driven by pore closing: a quantitative tomography investigation of structural formation in young C57BL/6 mice. *Acta Biomater* 22:92–102
82. Douissard P-A et al (2012) A versatile indirect detector design for hard X-ray microimaging. *J Instrum* 7(9):P09016–P09016

83. Golub EE (2009) Role of matrix vesicles in biomineralization. *Biochim Biophys Acta, Gen Subj* 1790(12):1592–1598
84. Vanleene M, Rey C, Ho Ba Tho MC (2008) Relationships between density and Young's modulus with microporosity and physico-chemical properties of Wistar rat cortical bone from growth to senescence. *Med Eng Phys* 30(8):1049–1056
85. Bach-Gansmo FL, Irvine SC, Brüel A, Thomsen JS, Birkedal H (2013) Calcified cartilage islands in rat cortical bone. *Calcif Tissue Int* 92(4):330–338
86. Shipov A, Zaslansky P, Riesemeier H, Segev G, Atkins A, Shahar R (2013) Unremodeled endochondral bone is a major architectural component of the cortical bone of the rat (*Rattus norvegicus*). *J Struct Biol* 183(2):132–140